THE ASTROPHYSICAL JOURNAL, 968:92 (9pp), 2024 June 20 https://doi.org/10.3847/1538-4357/ad4798

VODKA-JWST: A 3.8 kpc Dual Quasar at Cosmic Noon in a Powerful Starburst Galaxy with JWST/MIRI Integral Field Unit

Yu-Ching Chen[1], Yuzo Ishikawa[1], Nadia L. Zakamska[1], Xin Liu[2,3,4], Yue Shen[2], Hsiang-Chih Hwang[5], David Rupke[6], Andrey Vayner[1], Arran C. Gross[2], Weizhe Liu[7], Dominika Wylezalek[8], Sylvain Veilleux[9], Caroline Bertemes[8], Nadiia Diachenko[1], and Swetha Sankar[1]
[1] Department of Physics and Astronomy, Bloomberg Center, Johns Hopkins University, Baltimore, MD 21218, USA; ycchen@jhu.edu
[2] Department of Astronomy, University of Illinois at Urbana-Champaign, Urbana, IL 61801, USA
[3] National Center for Supercomputing Applications, University of Illinois at Urbana-Champaign, Urbana, IL 61801, USA
[4] Center for Artificial Intelligence Innovation, University of Illinois at Urbana-Champaign, 1205 West Clark Street, Urbana, IL 61801, USA
[5] School of Natural Sciences, Institute for Advanced Study, 1 Einstein Drive, Princeton, NJ 08540, USA
[6] Department of Physics, Rhodes College, 2000 N. Parkway, Memphis, TN 38112, USA
[7] Department of Astronomy, Steward Observatory, University of Arizona, Tucson, AZ 85719, USA
[8] Zentrum für Astronomie der Universität Heidelberg, Astronomisches Rechen-Institut, Mönchhofstr 12-14, D-69120 Heidelberg, Germany
[9] Department of Astronomy and Joint Space-Science Institute, University of Maryland, College Park, MD 20742, USA
Received 2024 March 4; revised 2024 April 30; accepted 2024 May 3; published 2024 June 14

Abstract

Dual quasars—two active supermassive black holes at galactic scales—represent crucial objects for studying the impact of galaxy mergers and quasar activity on the star formation rate (SFR) within their host galaxies, particularly at cosmic noon when SFR peaks. We present JWST/MIRI mid-infrared integral field spectroscopy of J074922.96+225511.7, a dual quasar with a projected separation of 3.8 kpc at a redshift $z = 2.17$. We detect spatially extended [Fe II] 5.34 μm and polycyclic aromatic hydrocarbon (PAH) 3.3 μm emissions from the star formation activity in its host galaxy. We derive the SFR of $10^{3.0\pm0.2}$ $M_\odot$ yr^{-1} using PAH 3.3 μm, which is 5 times higher than that derived from the knee of the infrared luminosity function for galaxies at $z \sim 2$. While the SFR of J0749+2255 agrees with that of star-forming galaxies of comparable stellar mass at the same redshifts, its molecular gas content falls short of expectations based on the molecular Kennicutt–Schmidt law. This discrepancy may result from molecular gas depletion due to the longer elevated stage of star formation, even after the molecular gas reservoir is depleted. We do not observe any quasar-driven outflow that impacts PAH and [Fe II] in the host galaxy based on the spatially resolved maps. From the expected flux in PAH-based star formation, the [Fe II] line likely originates from the star-forming regions in the host galaxy. Our study highlights the extreme stardust nature of J0749+2255, indicating a potential connection between the dual quasar phase and intense star formation activities.

Unified Astronomy Thesaurus concepts: Infrared astronomy (786); Double quasars (406); Active galactic nuclei (16); Galaxy mergers (608); Polycyclic aromatic hydrocarbons (1280); Star formation (1569)

1. Introduction

Most nearby galaxies host supermassive black holes (SMBHs) at their centers (Magorrian et al. 1998; Kormendy & Ho 2013), and hierarchical structure formation and galaxy mergers are anticipated in the cold dark matter universe (White & Frenk 1991; Navarro et al. 1996; Cole et al. 2000). Following galaxy mergers, SMBHs sink into the center of the merged galaxy and undergo evolution through dynamical friction (Yu 2002; Chen et al. 2020). Throughout this process, accretion via gas inflows can transform SMBHs into active galactic nuclei or quasars (Hopkins et al. 2008). When both SMBHs are simultaneously active, emitting electromagnetic radiation, the system becomes a dual quasar.

Identifying dual quasars on galactic scales, particularly at high redshifts ($z > 0.5$), is challenging due to angular resolution limitations (Figure 1 in Chen et al. 2022). Beyond $z > 0.5$, the separation of two quasars within $<1''$ (corresponding to $\lesssim 8$ kpc at $z = 1$) is below the typical resolving capability of ground-based optical/infrared telescopes. Conducting a systematic search for kiloparsec dual quasars at $z > 0.5$ using wide-field ground-based surveys is highly challenging, resulting in only a handful of such discoveries (Junkkarinen et al. 2001; Inada et al. 2012; More et al. 2016; Schechter et al. 2017; Lemon et al. 2018; Tang et al. 2021). Recently, the space-based Gaia survey has opened up new possibilities for finding kiloparsec dual quasars, leading to the discovery of dozens of candidates (Hwang et al. 2020; Chen et al. 2022; Mannucci et al. 2022). While some candidates proved to be star–quasar superpositions (Chen et al. 2022) or single quasars gravitationally lensed into multiple images (Gross et al. 2023; Li et al. 2023), follow-up observations using various facilities have confirmed the dual quasar nature for a few of them (Chen et al. 2023; Ciurlo et al. 2023).

Thanks to the high angular resolution (FWHM ranges from 0.″2 at 5.6 μm to 0.″8 at 25.5 μm) and sensitivity of the JWST, the spatially resolved mid-infrared (MIR) observations of quasar host galaxies have become possible (Rupke et al. 2023). Various MIR emission features, including those from the polycyclic aromatic hydrocarbons (PAHs), molecular hydrogen, and ionized gas, are diagnostic of gas physical conditions and excitation mechanisms in the host galaxies (Armus et al. 2006; Shi et al. 2007) and therefore afford the first opportunity to investigate the interplay between quasar fueling, quasar feedback, and star formation in its host.

To explore kiloparsec dual quasars in the MIR wavelengths for the first time, we perform JWST Mid-InfraRed Instrument (MIRI; Rieke et al. 2015) integral field unit (IFU) observations of a dual quasar, SDSSJ074922.96+225511.7 (hereinafter J0749+2255). This paper focuses on the analysis of MIRI data and on the study of detected emission features (e.g., [Fe II] 5.34μm and PAH 3.3 μm). We detail the observations, data reduction, and analysis in Section 2. We present the main results, including continuum maps, 1D spectra, and dynamics maps of [Fe II] and PAH emissions in Section 3. The study then delves into investigating the star formation rate using PAH 3.3 μm emission and whether [Fe II] solely originates from star formation in Section 4. We summarize our findings in Section 5.

2. Target Selection, Observations, Data Reduction, and Analysis

2.1. Our Target: J0749+2255

J0749+2255 is the first kiloparsec dual quasar at $z = 2.17$ with an identified host galaxy (Chen et al. 2023). It was initially discovered using its variability-induced astrometric noise (Shen et al. 2021; Chen et al. 2022). The selecting technique Varstrometry for Off-nucleus and Dual Sub-kiloparsec Active Galactic Nuclei (VODKA) utilizes the variability of quasars and the high astrometric accuracy of Gaia to find unresolved dual/lensed/off-nucleus quasars (Shen et al. 2019; Hwang et al. 2020). J0749+2255 was later confirmed as a dual quasar through multiwavelength observations (Chen et al. 2023). The spectra of both quasars in J0749+2255 are remarkably similar, and the Eddington ratios appear at least 0.1 (Chen et al. 2023). J0749+2255 shows faint tidal tails in the deep Hubble Space Telescope (HST) near-IR images, as an indicator of a merging system (Chen et al. 2023). However, recent JWST NIRSpec IFU observations reveal a giant rotating disk perpendicular to the direction of two nuclei, rather than a disturbed system with irregular merger morphology (Y. Ishikawa et al. 2024). Moreover, the [O III] emission appears faint, and there is no indication of robust galactic winds in the ionized gas (Y. Ishikawa et al. 2024). All those findings make the formation of J0749+2255 and its relation with the host galaxy an intriguing topic.

2.2. JWST MIRI/MRS Data Reduction

J0749+2255 was observed as part of JWST-GO-02654 (PI: Ishikawa) with the Medium Resolution Spectrometer (MRS) mode of the MIRI instrument on JWST on 2022 November 21–22 UT (Argyriou et al. 2023). The data were acquired in the long grating mode, which covers the wavelength range of 6.53–7.65 μm, 10.02–11.70 μm, 15.41–17.98 μm, and 24.19–27.90 μm in four channels. The observations utilized a 4-point dither pattern to enhance sampling and achieve improved spatial resolution in the final drizzled data cube (Law et al. 2023). Dedicated background exposures were simultaneously taken in the nearby field from the target position for background subtraction. All the JWST data used in this paper can be found at MAST doi:10.17909/hh7a-c798.

We process the data using JWST calibration pipeline version 1.11.4 (Bushouse et al. 2023). In the first stage, the `Detector1` pipeline applies detector-level corrections to all uncalibrated science and background exposures, converting raw images into corrected count rate files. These count rate files are then processed with the `Spec2` pipeline, which performs various instrument-specific calibrations, including wavelength calibration, flat-field correction, flux calibration, fringing removal, and other calibrations (Labiano et al. 2021). We apply image-by-image background subtraction using background exposures taken simultaneously to account for flat-field correction and pixel-by-pixel variation in the detectors, rather than the default 1D master background subtraction. The `Spec2` pipeline converts count rate files into fully calibrated individual exposures. In the `Spec3` pipeline, calibrated individual exposures across different wavelength bands and channels are combined into the final 3D drizzled data cubes. Following the standard pipeline procedure, we eliminate faint strip patterns using procedures outlined in Spilker et al. (2023). The stripe patterns were modeled using 2D background templates derived from the moving average of the data cube along the wavelength direction, with regions near the dual quasar excluded when creating the stripe templates.

2.3. q3dfit Fitting

Revealing the faint emission from the host galaxy on top of the strong quasar emission might require specialized treatment, involving dedicated point-spread function (PSF) subtraction and spectral decomposition techniques. In the analysis of J0749+2255, we use the `q3dfit` software (Rupke 2014; Rupke et al. 2021), available for JWST through the Early-Release Science program ERS-01335 "Q3D". `q3dfit` is capable of decomposing the emission of the quasar from that of the host galaxy and conducting spectral fitting for JWST IFU data cubes. This tool has been utilized to study gas kinematics in quasar host galaxies in IFU data obtained with the JWST (Wylezalek et al. 2022; Rupke et al. 2023; Vayner et al. 2023) and from the ground (Rupke et al. 2017). Though `q3dfit` possesses the capability for PSF subtraction, we opt not to utilize it in this case. This decision is based on the observation that neither the PAH 3.3 μm emission nor the [Fe II] 5.34μm emission is dominated by the quasars, in that there is not a strong PSF component associated with the nuclei that would swamp the emission from the host.

To separate PAH 3.3 μm features from the dust continuum, we fit the spectrum using a linear combination of a modified blackbody function, representing the warm dust emission from the quasar's dusty torus, and the PAH template from Lai et al. (2020). This fitting is applied to the spectra in Channel 2 (10–11 μm) at each spaxel. `q3dfit` uses a linear combination of predefined PAH templates to measure the contribution of PAHs to the MIR spectra, with only one fitting parameter, the amplitude, for each template. In practice, at wavelength <5 μm (the wavelength range not covered by Spitzer observations), only one template from AKARI is available, which fits the 3.3 μm PAH feature with a linear combination of three Drude profiles (Lai et al. 2020). The Drude profile is a theoretical profile for a classical damped harmonic oscillator, which is suitable for modeling PAH emission features (Smith et al. 2007). The flux of the PAH 3.3 μm feature is obtained by integrating the flux density of the PAH template between 3.2 μm and 3.35 μm. For the [Fe II] 5.34μm line, we perform a local fit within a narrow wavelength range (16.65–17.2 μm) in Channel 3. The continuum is modeled with a third-degree polynomial, and the [Fe II] line is modeled with a single Gaussian function.

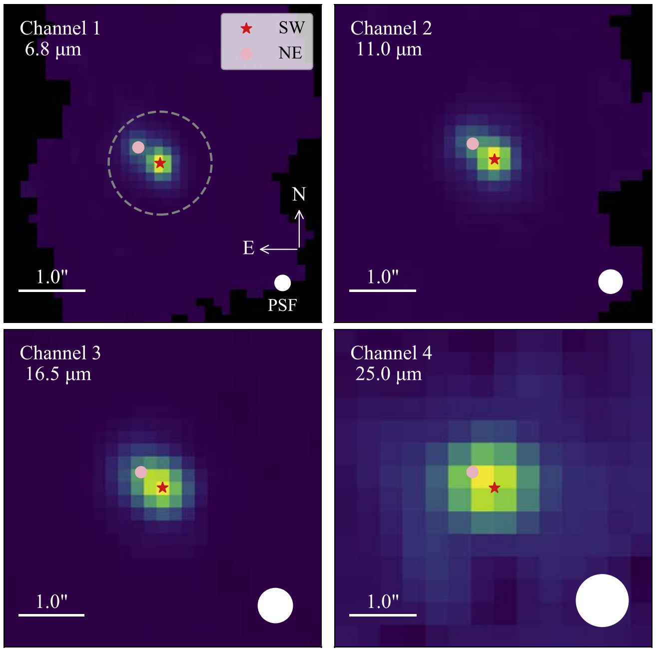

Figure 1. MIR continuum images of J0749+2255 in the four channels. The color indicates the flux in the linear scale. The positions of the quasars are indicated with pink circles and red stars. Two quasars are already marginally resolved in Channel 1. The black areas represent regions outside the MIRI field of views. White-filled circles represent the FWHM of the PSFs. A gray dashed circle denotes the aperture size utilized for extracting the spectra in Figure 2.

Table 1
Continuum Luminosities of Two Nuclei and Flux Ratios at Each Channel

Wavelength (μm)	$\log(\lambda L_{\lambda,\mathrm{SW}})$ (erg s^{-1})	$\log(\lambda L_{\lambda,\mathrm{NE}})$ (erg s^{-1})	Flux Ratio
6.8	45.44 ± 0.04	45.11 ± 0.08	2.1 ± 0.4
11.0	45.55 ± 0.03	45.26 ± 0.06	1.9 ± 0.3
16.5	45.52 ± 0.03	45.22 ± 0.06	2.0 ± 0.3
25.0	45.58 ± 0.10	45.37 ± 0.17	1.6 ± 0.7

Note. The errors are 1σ statistical uncertainties.

3. Results

3.1. MIR Continuum Maps and Spectra

Figure 1 shows MIR continuum images of J0749+2255 obtained from MIRI. Continuum maps were generated by averaging spectra within emission-line-free wavelength ranges. At the shortest wavelength of 7 μm, with an angular resolution of ∼0.″3 and a quasar separation of 0.″46, the dual quasar is marginally resolved in Channel 1. At longer wavelengths, the two nuclei appear blended into an elongated source due to lower spatial resolution. We use 2D Gaussian functions to fit the continuum images, with fixed positions and FWHM. The positions of the quasars were determined using the Channel 1 map because of its better spatial resolution, and the FWHM values were derived from diffraction-limited PSFs (Rigby et al. 2023). Table 1 lists the fitted luminosities of two nuclei and their flux ratios.

Subsequently, we extract the 1D spectra for each channel using a circular region with a diameter of 0.″8 centered at the southwestern nuclei to identify the possible emission lines. We observe strong PAH features at 3.3 μm and a significant [Fe II] 5.34μm line. Figure 2 displays the 1D spectra of J0749+2255 centered at the PAH 3.3 μm features and the [Fe II] 5.34μm line.

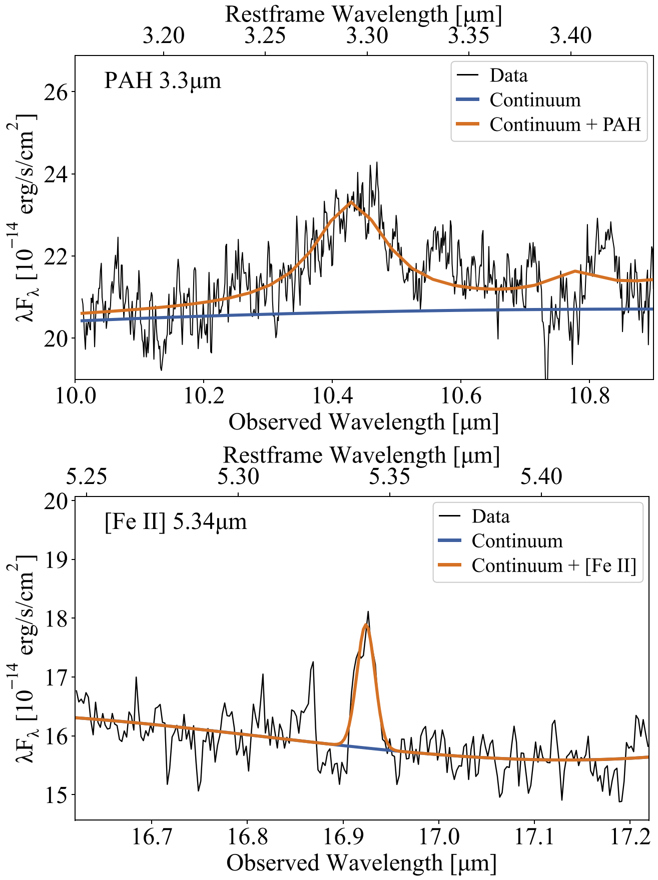

Figure 2. The 1D extracted MIR spectra of J0749+2255 centered at the PAH 3.3 μm feature (top) and the [Fe II] 5.34μm line (bottom). The spectra are for the entire system enclosed by the 0.″8 extraction aperture. The fitted models including a continuum, a PAH template, and/or a Gaussian component are also plotted.

We also plot the fitted models on top of the data. Besides the PAH 3.3 μm features and the [Fe II] 5.34μm line, a faint PAH feature at 5.24 μm and a faint rotational line of molecular hydrogen, H_2 00 S(7), are likely detected. However, the fluxes of PAH 5.24 μm and H_2 00 S(7) are only slightly above the noise level, so we do not conduct further analysis for them. In the subsequent sections, we focus on PAH 3.3 μm and [Fe II] 5.34μm exploring their morphology, line intensity, and dynamics.

3.2. PAH 3.3 μm Map

We separate the PAH 3.3 μm features from the dust continuum in Channel 2, as detailed in Section 2.3. Figure 3 shows the resulting PAH luminosity map. The PAH emission extends spatially out to approximately 10 kpc in diameter, particularly around the NE nucleus. The typical signal-to-noise ratios (SNR) per spaxel are 5–10 within the 5 kpc radius. By summing the luminosity within a radius of 1.″5 (equivalent to 12 kpc) at the center of the two nuclei, we find that the total luminosity of the PAH 3.3 μm feature is $L_{\mathrm{PAH\ 3.3}} = 10^{9.8\pm0.1}$ $L_{\odot}$. The error represents 1σ systematic uncertainty based on fitting residuals, absolute flux calibration, and the accuracy of templates.

3.3. [Fe II] Line Map

Figure 4 shows [Fe II] 5.34 μm luminosity and velocity centroid maps. After subtracting the continuum, we find that

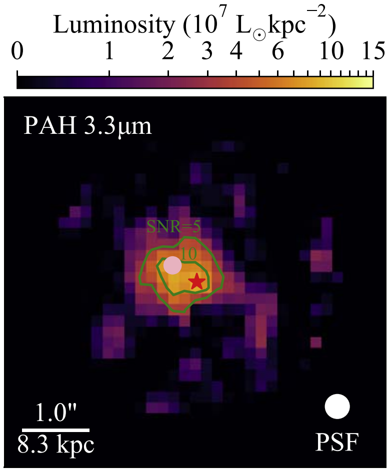

Figure 3. Integrated PAH 3.3 μm luminosity map of J0749+2255 in units of 10^7 $L_\odot$ kpc^{-2}. The solid green contours represent signal-to-noise ratios (SNR) of 5 and 10. Spaxels close to the edges of IFU are masked to avoid the artifact features. North is up, and east is to the left.

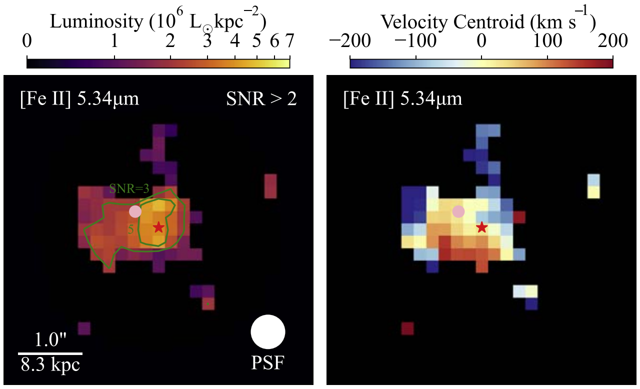

Figure 4. Left: line-integrated [Fe II] 5.34μm luminosity map of J0749+2255 in units of 10^6 $L_\odot$ kpc^{-2}. Right: radial velocity centroid map in units of km s^{-1}. The solid green contours represent SNRs of 3 and 5. Spaxels close to the edges of IFU are masked to avoid the artifact features. Spaxels with [Fe II] SNR < 2 are also masked. North is up, and east is to the left.

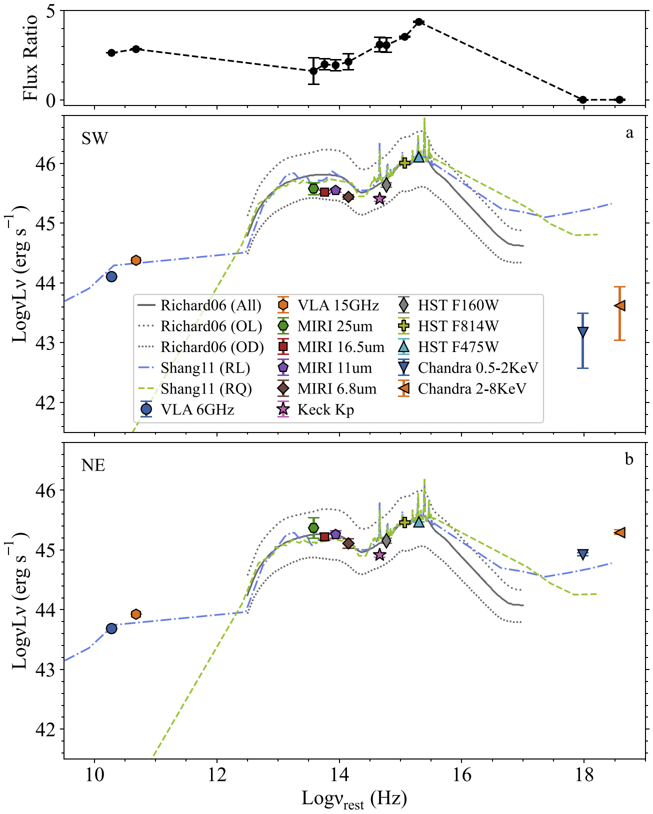

Figure 5. Top: SW/NE flux ratios between two nuclei. Middle and bottom: SEDs of SW and NE nuclei in J0749+2255. MIRI data points, along with multiwavelength observations from Chen et al. (2023), are plotted. The gray curves represent the SEDs of optically selected Sloan Digital Sky Survey quasars (Richards et al. 2006), with solid lines showing mean values and dotted lines indicating optically luminous and dim subpopulations. Additional SEDs are from Shang et al. (2011), covering both radio-loud and radio-quiet populations. The comparison templates are normalized to match the respective luminosities in the F814W filter of HST observations.

the [Fe II] emission exhibits an extended structure with a diameter of approximately 10 kpc. The typical SNRs of the [Fe II] line per spaxel are 3–5. The [Fe II] line is spectrally unresolved, with a typical fitted FWHM of ∼150 km s^{-1}, close to the spectral resolution of MIRI at 17 μm (Labiano et al. 2021). The velocity centroid map reveals an extended structure that is blueshifted toward the northwest and redshifted toward the southeast, with the velocity gradient perpendicular to the direction of the two nuclei. The radial velocities of the blueshifted and redshifted components are approximately 100–200 km s^{-1}. A similar kinematic pattern is also observed in the Hα map, which is interpreted by Y. Ishikawa et al. (2024) as due to galaxy rotation. Using a 1$''\!.$5 radius aperture centered at the middle of two nuclei, we obtain the total luminosity of the [Fe II] line $L_{\rm [Fe\ II]} = 10^{8.72\pm0.05}$ $L_\odot$. The error represents 1σ systematic uncertainty based on fitting residuals and absolute flux calibration.

4. Discussion

4.1. Spectral Energy Distribution

Leveraging the high angular resolution of the JWST, we successfully separate the MIR continuum emissions of two nuclei. By incorporating values from Table 1 and multiwavelength observations from Chen et al. (2023), we present the spectral energy distributions (SEDs) of both nuclei in J0749+2255 in Figure 5. Both SEDs are dominated by emission from quasar and consistent with unobscured quasar templates (Richards et al. 2006; Shang et al. 2011), showing bumps in ultraviolet and MIR wavelengths. Previous radio observations revealed that the two nuclei both have very high radio luminosity of $\nu L_\nu \sim 10^{43-44}$ erg s^{-1} (Chen et al. 2023). Combined with optical luminosity, the radio loudnesses $R_{6\ {\rm cm}/2500\ {\rm \mathring{A}}}$, defined as the flux ratio at the rest frame 6 cm and that at 2500 Å, are more than 600. Our SEDs highlight the quasar-dominant and radio-loud nature of both nuclei.

The SW/NE flux ratios in J0749+2255 consistently decrease from 4.4 to 1.6 from rest-frame UV to MIR wavelengths. Then, the ratio rises to 2.8 in radio wavelengths. We already know from HST near-IR and Chandra X-ray observations that our target is most consistent with being a dual quasar rather than a lensed quasar (Chen et al. 2023). Barring dramatic variability, any differences between the SEDs of the two quasars indicate that they comprise a physical quasar pair rather than a lensed quasar. The X-ray flux ratios are significantly lower (≪1), further diminishing the likelihood of a lensed quasar scenario. Wavelength-dependent geometry

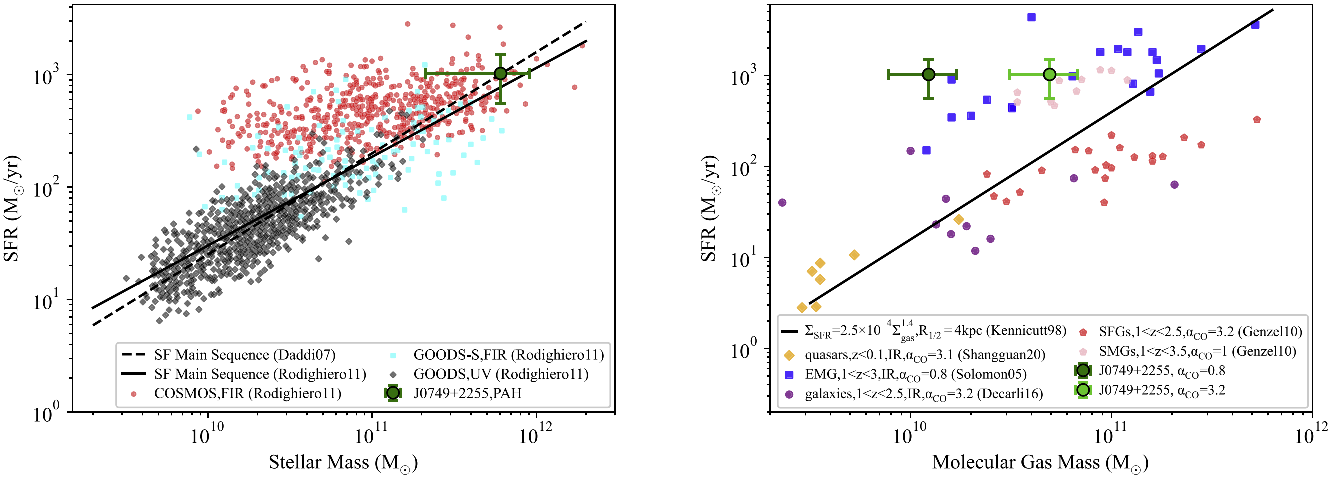

Figure 6. Left: SFR vs. stellar mass of host galaxy for J0749+2255 in comparison to the main sequence of star-forming galaxies. The red circles, cyan squares, and black diamonds are star-forming galaxies at $1.5 < z < 2.5$ in COSMOS and GOODS fields using UV- or far-infrared-based SFR (Rodighiero et al. 2011). The black dashed and solid lines represent the main sequence of star-forming galaxies (Daddi et al. 2007; Rodighiero et al. 2011). Right: SFR vs. gas (H_2+He) mass of the host galaxies for J0749+2255 in comparison to different galaxy/quasars/submillimeter galaxy samples. The black line represents the molecular Kennicutt–Schmidt law $\Sigma_{\rm SFR} = 2.5\times10^{-4}\Sigma_{\rm gas}^{1.4}$ (Kennicutt 1998). We use the half-light radius $R_{1/2} = 4$ kpc and calculate the molecular gas mass $M_{\rm mol-gas} = 2 \times \pi R_{1/2}^2 \Sigma_{\rm mol-gas}$. The orange diamonds are local PG quasars (Shangguan et al. 2020). The blue squares are emission line galaxies (EMGs) at $1 < z < 3$ (Solomon & Vanden Bout 2005). The red and pink hexagons are star-forming galaxies (SFGs) and submillimeter galaxies (SMGs) at $1 < z < 3.5$ (Genzel et al. 2010). The purple circles are CO-detected galaxies at $1 < z < 2.5$ in the Hubble Ultra Deep Field (Decarli et al. 2016). The CO-to-H_2 conversion factor α_{CO} used in each sample is also shown.

or extinction in a lensed galaxy could introduce chromatic effects (Pooley et al. 2007; Barnacka et al. 2014), but the observed variations from X-ray to radio wavelengths make the lensed quasar scenario very unlikely.

4.2. Star Formation Rate Based on 3.3 μm PAH

PAH emission serves as an effective calorimeter for star formation rate (SFR; Förster Schreiber et al. 2004; Peeters et al. 2004), even in quasar host galaxies where finding SFR measures unaffected by quasar radiation is very difficult (Zakamska et al. 2016). Ultraviolet photons from hot stars heat up PAH molecules, causing them to re-emit radiation in specific MIR bands through vibration (Puget & Leger 1989). Measures of SFR typically rely on stronger PAH features at longer wavelengths (e.g., 6.2, 7.7, and 11.3 μm) for both quasar hosts (Shi et al. 2007; Zakamska et al. 2016) and star-forming galaxies (Shipley et al. 2016; Xie & Ho 2019). Because of the sensitivity and wavelength coverage limitations of the Spitzer telescope, studies of SFR indicators using 3.3 μm PAH remain scarce, especially for quasar hosts (Kim et al. 2012; Lai et al. 2020). We use the calibration of SFR for the 3.3 μm PAH from Equation (1) in Lai et al. (2020),

$$\log\left(\frac{\rm SFR}{M_\odot {\rm yr}^{-1}}\right) = -(6.80 \pm 0.18) + \log\left(\frac{L_{\rm PAH\ 3.3}}{L_\odot}\right), \quad (1)$$

to compute the PAH-based SFR. The estimated total SFR for J0749+2255 is $10^{3.0\pm0.2}\ M_\odot\ {\rm yr}^{-1}$. The 1σ error is dominated by the uncertainty in the conversion between PAH and SFR (Lai et al. 2020). The SFR of J0749+2255 is very high, $\sim$5 times higher than that derived from the knee luminosity $L_{\rm knee}$ of the infrared luminosity function for galaxies at $z \sim 2$ (Magnelli et al. 2013). The extreme starburst nature resembles that of submillimeter galaxies and emission line galaxies observed at cosmic noon (Barger et al. 1998; Hughes et al. 1998; Solomon & Vanden Bout 2005; Genzel et al. 2010).

The SFR based on the 3.3 μm PAH could be underestimated because small PAHs, traced by the PAH feature at shorter wavelengths as compared to the canonical 6.2 and 7.7 μm diagnostics, may be destroyed by the strong radiation from quasars (Diamond-Stanic & Rieke 2010; Wu et al. 2010). Recent JWST/MIRI IFU observation of a $z = 4.22$ lensed submillimeter galaxy reveals a spatial mismatch between PAH 3.3 μm and far-IR emission, demonstrating that PAH 3.3 μm might not be a good direct indicator of the star formation rate of high-redshift galaxies (Spilker et al. 2023). However, some studies found no decline in the 3.3 μm PAH intensity relative to the total PAH intensity at the high luminosity end in star-forming galaxies, suggesting that the smallest PAHs may survive in strong radiation fields (Lai et al. 2020).

SFR can also be estimated from various other indicators such as Hα. The total SFR estimated from Hα using the JWST NIRSpec is $\sim$1700 $M_\odot$ yr^{-1} (Y. Ishikawa et al. 2024). The Hα-based SFR is consistent with the PAH-based SFR given the typical 1σ systematic error of 0.2 dex. Shipley et al. (2016) found a tight correlation between PAH luminosity and the extinction-corrected Hα luminosity for 105 galaxies at $0 < z < 0.4$ over a wide range of luminosities, suggesting that the PAH features may be as accurate an SFR indicator as hydrogen recombination lines. The PAH map of J0749+2255 does not show strong contribution from the quasars and no strong quasar outflow is seen, so we do not expect a strong bias of PAH-based SFR due to quasars.

4.3. Stellar Mass–SFR Relation and Kennicutt–Schmidt Law

We can combine the SFR estimated from PAH 3.3 μm with other physical properties of host galaxies (e.g., stellar mass and molecular gas mass) to investigate whether kiloparsec dual quasars like J0749+2255 have enhanced or suppressed SFR. Using the estimated combined host galaxy mass of $10^{11.78}\ M_\odot$ from the F160W images obtained with the HST (Chen et al. 2023), we derive the specific SFR as 1.7×10^{-9} yr^{-1}. In Figure 6, left, compared to the empirical stellar mass–SFR relations of single galaxies, J0749+2255 resides on the luminous end of the main sequence for star-forming galaxies at $z \sim 2$ (Daddi et al. 2007; Rodighiero et al. 2011). The highly star-forming nature of J07492+2255 is very intriguing because our target selection is not based on any of the galaxy properties.

In addition to exploring the stellar mass–SFR relationship, we also investigate whether J0749+2255 adheres to the molecular gas Kennicutt–Schmidt law (Schmidt 1959; Kennicutt 1998; Kennicutt & Evans 2012). The molecular hydrogen H_2 mass is derived from recent Atacama Large Millimieter/submillimeter Array CO (4-3) observations (Y. Ishikawa et al. 2024). We obtain the total line-integrated flux $S_{\rm CO}\Delta v$ of J0749+2255 in the unit of Jy km s^{-1} and convert it to the intrinsic CO luminosity $L'_{\rm CO}$ using the following equation:

$$L'_{\rm CO} = 3.25 \times 10^7 S_{\rm CO}\Delta v \frac{D_L^2}{(1+z)^3 \nu_{\rm obs}^2} {\rm K\ kms^{-1}\ pc^2}, \qquad (2)$$

where D_L is the luminosity distance in Mpc, z is the redshift, and $\nu_{\rm obs}$ is the observed frequency in GHz. We assume that the low-J CO transitions are thermalized and optically thick, so $R_{41} = L'_{\rm CO\,4-3}/L'_{\rm CO\,1-0} \sim 1$. We use $R_{41} = 0.87$ obtained from local quasars (Carilli & Walter 2013). We also include a factor of 1.36 for helium to compute the molecular gas mass. We assume the CO luminosity-to-H_2 mass conversion factor $\alpha_{\rm CO}$ of 0.8 (Solomon & Vanden Bout 2005; Tacconi et al. 2008), though the systematic uncertainty could be at least 30% (Papadopoulos et al. 2012; Bolatto et al. 2013). The molecular gas mass can be calculated as

$$M_{\rm mol-gas} = 1.36\alpha_{\rm CO} R_{41}^{-1} L'_{\rm CO\,4-3}. \qquad (3)$$

The estimated molecular gas mass is $10^{10.09\pm0.16}\ M_\odot$. At the current SFR, the resulting depletion time, where all molecular gas would be consumed, is only 10 Myr. We plot SFR as a function of gas mass for J0749+2255 (Figure 6), in comparison to local quasars (Shangguan et al. 2020), various galaxy samples at $z \sim 2$ (Solomon & Vanden Bout 2005; Genzel et al. 2010; Decarli et al. 2016), and the molecular Kennicutt–Schmidt law (Kennicutt 1998). We find that J0749+2255 exhibits higher (∼5–20 times) SFR compared with those samples with the same amount of molecular gas. Even if we consider a higher CO-to-H_2 conversion factor $\alpha_{\rm CO}$ of 3.2, J0749+2255 is still an outlier from the Kennicutt–Schmidt law at its redshift.

We discuss the possible reasons for the deviation. PAH-based SFR could be biased (Spilker et al. 2023); however, the good agreement between PAH-based and Hα-based SFR makes this scenario unlikely. Even if PAHs are affected by quasars, the feedback from quasars is usually negative (Diamond-Stanic & Rieke 2010; Xie & Ho 2019) and we do not observe any paucity of PAHs around the quasars. The destruction of PAHs would make the discrepancy even worse.

Therefore, the deviation from the Kennicutt–Schmidt law could originate from the enhancement of SFR or depletion of molecular gas due to mergers or quasars. Merging galaxies are thought to trigger episodes of extreme star formation (Barnes 2004; Saitoh et al. 2009), though some observations suggest the enhancement of SFR due to mergers is moderate, with a factor of 2–3, or not significant (Ellison et al. 2013; Knapen et al. 2015; Silva et al. 2018; Pearson et al. 2019). Quasars have been known to both suppress and trigger star formation in their host galaxies (Cresci & Maiolino 2018). The outflow from the quasar could also destroy or expel the molecular gas reservoir (Schawinski et al. 2009). Nevertheless, the outflow from quasars is weak in J0749+2255 based on the [Fe II] map and the [O III] analysis (Y. Ishikawa et al. 2024), thus the contribution from the quasar might not be significant. One potential explanation is that the elevated stage of star formation has persisted for an extended duration, without diminishing even as the molecular gas reservoir is gradually depleted.

To sum up, the high SFR rate of J0749+2255 suggests possible enhancement of SFR during the dual quasar stage. These starburst activities could be supported by simulations or calculations showing enhanced star formation in interacting galaxies (Knapen et al. 2015; Moreno et al. 2019) or during the quasar stage (King 2005). Though whether two quasars are a result of a merger or born in the same massive galaxy is still in debate (Y. Ishikawa et al. 2024), the connection between dual quasars and high SFR is striking because our target selection is not based on galaxy properties.

4.4. [Fe II] Is Likely Driven by Star Formation

[Fe II] lines observed at the IR wavelengths are commonly associated with shock-heated nebulae, such as supernova remnants and young stellar objects (Greenhouse et al. 1991; Nisini et al. 2002). These shocks can destroy grains, causing iron atoms in the dust grain to be sputtered into the gas phase and ionized by the radiation field (Mouri & Taniguchi 2000). Quasar-driven outflows may also generate shocks when interacting with the neutral interstellar medium, leading to strong [Fe II] emission (Hill & Zakamska 2014). Our aim here is to examine whether the observed [Fe II] 5.34μm line is attributed to quasars or star formation within the host galaxies. To address this, we utilize the SFR derived from the 3.3 μm PAH to calculate the supernova rate and subsequently convert it into an anticipated [Fe II] luminosity originating solely from the host galaxy star formation.

The relationship between SFR and supernova (SN) rate $\nu_{\rm SN}$ in the host galaxy can be expressed by

$$\frac{\nu_{\rm SN}}{\rm SFR} = \frac{\int_{M_{L,\rm SN}}^{M_U} \frac{{\rm d}N}{{\rm d}M} {\rm d}M}{\int_{M_{L,\rm SFR}}^{M_U} M \times \frac{{\rm d}N}{{\rm d}M} {\rm d}M}, \qquad (4)$$

where M is the mass of a star, $\frac{{\rm d}N}{{\rm d}M}$ is the initial mass function, $M_{L,\rm SN}$ is the lower mass limit of stars that become SN, and $M_{L,\rm SFR}$ is the lower mass limit of stars that contribute to the SFR. We assume that the PAH-based SFR arises from all stars with a mass higher than 2 $M_\odot$(Peeters et al. 2004), that stars with a mass higher than 8 $M_\odot$ eventually lead to supernovae, and that the initial mass function is truncated at $M_U = 100 M_\odot$. Using the Salpeter initial mass function with $dN/dM \propto M^{-\alpha}$ with $\alpha = -2.35$ (Salpeter 1955), the estimated SN rate based on PAH-derived SFR is 27 yr^{-1}.

Rosenberg et al. (2012) find a tight relation between [Fe II] 1.26 μm and SN rate in a sample of nearby galaxies. By incorporating the estimated SN rate into this correlation, we derive the anticipated [Fe II] 1.26 μm luminosity of $L_{\rm [Fe\ II]1.26\mu m} = 10^{8.6}\ L_\odot$, originating solely from star-forming regions within the host galaxies. While the relative strength of the [Fe II] 5.34 μm line and the [Fe II] 1.26 μm lines remains

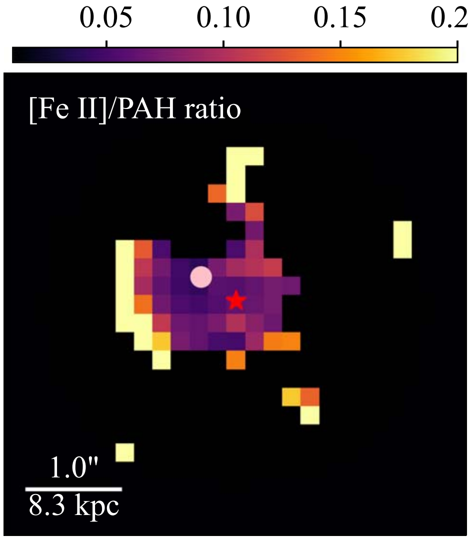

Figure 7. [Fe II] 5.34 μm/PAH 3.3 μm flux ratio map. Spaxels close to the edges of IFU are masked to avoid the artifact features. Spaxels with [Fe II] signal-to-noise ratio (SNR) <2 are masked. North is up, and east is to the left.

uncertain for J0749+2255, observations of supernova remnants (Reach et al. 2006) and simulations of radiative shocks (Hartigan et al. 2004) suggest that these lines should have comparable fluxes. We estimate the systematic uncertainty of 0.4 dex for the expected [Fe II] 5.34μm luminosity using different assumptions. Under the assumption of equal fluxes between the [Fe II] 5.34 μm and the [Fe II] 1.26 μm the observed [Fe II] 5.34μm luminosity of $10^{8.7}$ $L_\odot$ agrees well with the anticipated [Fe II] luminosity of $10^{8.6}$ $L_\odot$ originating from star-forming regions in the host galaxy. Furthermore, the kinematics of [Fe II] presented in Figure 4 are consistent with the rotational disk morphology observed in Hα (Y. Ishikawa et al. 2024). Hence, we conclude that the [Fe II] 5.34 μm emission of J0749+2255 is primarily associated with star formation rather than with the quasars. Future JWST observations in near-infrared and MIR wavelengths with various quasar samples will probe the origin of [Fe II] and whether [Fe II] can be used as a shock/feedback diagnostic.

4.5. Spatially Resolved [Fe II]/PAH Map

Utilizing the spatially resolved [Fe II] 5.34μm and PAH 3.3 μm map of J0749+2255, we aim to explore the spatial variations in the [Fe II]/PAH ratio. To this end, we reproject and convolve the PAH map with a 2D Gaussian kernel to match the pixel scales and the PSF size in the [Fe II] map. The resulting [Fe II]/PAH ratio map is shown in Figure 7. According to the calculations in Section 4.4, the anticipated [Fe II]/PAH flux ratio from star formation is approximately 0.16. In the host galaxy of J0749+2255, the [Fe II]/PAH ratios range between 0.05 and 0.2, broadly consistent with the expected value. Contrary to expectations, there is no observable increase in [Fe II]/PAH ratios at both nuclei, as would be anticipated from enhanced [Fe II] emission because of quasar-driven shocks (Hill & Zakamska 2014) or the disruption of small PAH molecules by the strong radiation from quasars (Diamond-Stanic & Rieke 2010; Wu et al. 2010). We conclude that neither the radiation field of the quasars nor quasar-driven outflows penetrate sufficiently into the gas-rich host galaxy, and therefore there is no detectable spatially resolved sign of either radiative suppression of PAHs or quasar-driven shocks that would enhance [Fe II]. This is in line with other observations of J0749+2255, which demonstrate the lack of evidence from quasar-driven outflow tracers such as [O III] (Y. Ishikawa et al. 2024).

5. Conclusions

In this study, we present high spatial resolution MIR IFU observations of a 3.8 kpc dual quasar at $z = 2.17$. Our analysis involves extracting the MIR continuum luminosity for each quasar, leading to the construction of their SEDs. The SEDs of both quasars align with the characteristics of typical optically selected radio-loud quasars (Figure 5). Additionally, we identify and characterize strong spatially extended features, including the PAH 3.3 μm feature and the [Fe II] 5.34 μm line, as shown in Figure 3 and Figure 4, respectively. We see the rotation of the host galaxy in the [Fe II] 5.34 μm map, consistent with that seen in other tracers (e.g., Hα).

By leveraging the PAH 3.3 μm feature, we estimate an SFR of $10^{3.0\pm0.2}$ $M_\odot$ yr^{-1} for J0749+2255, placing it in a category of extreme starburst galaxies. When combined with the stellar mass, the specific SFR of J0749+2255 is 1.7×10^{-9} yr^{-1}, similar to star-forming galaxies at redshift $z \sim 2$ (Figure 6), which is exceptional given J07492+2255 was not selected based on its host galaxy properties. Using the molecular gas mass estimated from CO, we find that the SFR of J0749+2255 is $\gtrsim$10 times higher than the molecular Kennicutt–Schmidt law or the comparison samples with the same amounts of molecular gas. The deviation could be related to the prolonged stage of high star formation, persisting even as the molecular gas reservoir is depleted.

To investigate the origin of the [Fe II] emission, whether driven by star formation or quasar outflows, we calculate the expected [Fe II] luminosity solely from star formation and compare it with the observed value. The observed and expected [Fe II] luminosities agree, suggesting that the predominant source of [Fe II] emission is likely star formation within the host galaxy. Additionally, no noticeable small-scale quasar-driven wind signatures are observed in the spatial variation of the [Fe II]/PAH map (Figure 7). We do not detect any rise in [Fe II]/PAH ratio around quasars that could be related to quasar-driven wind. Based on our analysis of [Fe II] and PAH, we conclude that both quasars in J0749+2255 do not exhibit strong outflows that significantly impact the host galaxy, consistent with observations from other outflow tracers.

In summary, we discover that the 3.8 kpc dual quasar, J0749+2255, resides in a powerful starburst galaxy using the PAH 3.3 μm observation. The extremely high SFR reveals a possible connection between star formation activities and the dual quasar phase. The lower molecular gas mass in J0749+2255, compared with the molecular Kennicutt–Schmidt law, suggests the elevated stage of star formation might have persisted for an extended duration, even after the molecular gas reservoir is depleted. Our study demonstrates the capability of JWST to conduct spatially resolved MIR observations for kiloparsec-scale dual quasars. We anticipate that future JWST MIR observations on a larger sample of dual quasars will provide a statistically robust understanding of how kiloparsec-scale dual quasars influence star formation and molecular gas within host galaxies.

Acknowledgments

This work is based on observations made with the NASA/ESA/CSA James Webb Space Telescope. The data were obtained from the Mikulski Archive for Space Telescopes at the Space Telescope Science Institute, which is operated by the Association of Universities for Research in Astronomy, Inc., under NASA contract NAS 5-03127 for JWST. These observations are associated with program #2654. Support for programs GO-02654 and ERS-01335 (N.L.Z., D.R., A.V., S. V., and S.S.) was provided by NASA through grants from the Space Telescope Science Institute, which is operated by the Association of Universities for Research in Astronomy, Inc., under NASA contract NAS 5-03127. This work is supported by the Heising-Simons Foundation and Research Corporation for Science Advancement, and NSF grant AST-2108162 (X.L., Y. S., and A.G.).

Facility: JWST (MIRI)

Software: astropy (Astropy Collaboration et al. 2013, 2018, 2022), reproject (Robitaille et al. 2023) `q3dfit` (Rupke 2014; Rupke et al. 2021).

ORCID iDs

Yu-Ching Chen https://orcid.org/0000-0002-9932-1298
Yuzo Ishikawa https://orcid.org/0000-0001-7572-5231
Nadia L. Zakamska https://orcid.org/0000-0001-6100-6869
Xin Liu https://orcid.org/0000-0003-0049-5210
Yue Shen https://orcid.org/0000-0003-1659-7035
Hsiang-Chih Hwang https://orcid.org/0000-0003-4250-4437
David Rupke https://orcid.org/0000-0002-1608-7564
Andrey Vayner https://orcid.org/0000-0002-0710-3729
Arran C. Gross https://orcid.org/0000-0001-7681-9213
Weizhe Liu https://orcid.org/0000-0003-3762-7344
Dominika Wylezalek https://orcid.org/0000-0003-2212-6045
Sylvain Veilleux https://orcid.org/0000-0002-3158-6820
Caroline Bertemes https://orcid.org/0000-0002-6948-1485
Nadiia Diachenko https://orcid.org/0009-0003-5128-2159
Swetha Sankar https://orcid.org/0000-0002-4419-8325

References

Argyriou, I., Glasse, A., Law, D. R., et al. 2023, A&A, 675, A111
Armus, L., Bernard-Salas, J., Spoon, H. W. W., et al. 2006, ApJ, 640, 204
Astropy Collaboration, Price-Whelan, A. M., Lim, P. L., et al. 2022, ApJ, 935, 167
Astropy Collaboration, Price-Whelan, A. M., Sipőcz, B. M., et al. 2018, AJ, 156, 123
Astropy Collaboration, Robitaille, T. P., Tollerud, E. J., et al. 2013, A&A, 558, A33
Barger, A. J., Cowie, L. L., Sanders, D. B., et al. 1998, Natur, 394, 248
Barnacka, A., Geller, M. J., Dell'Antonio, I. P., & Benbow, W. 2014, ApJ, 788, 139
Barnes, J. E. 2004, MNRAS, 350, 798
Bolatto, A. D., Wolfire, M., & Leroy, A. K. 2013, ARA&A, 51, 207
Bushouse, H., Eisenhamer, J., Dencheva, N., et al. 2023, WST Calibration Pipeline, v1.11.4, Zenodo, doi:10.5281/zenodo.8247246
Carilli, C. L., & Walter, F. 2013, ARA&A, 51, 105
Chen, Y., Yu, Q., & Lu, Y. 2020, ApJ, 897, 86
Chen, Y.-C., Hwang, H.-C., Shen, Y., et al. 2022, ApJ, 925, 162
Chen, Y.-C., Liu, X., Foord, A., et al. 2023, Natur, 616, 45
Ciurlo, A., Mannucci, F., Yeh, S., et al. 2023, A&A, 671, L4
Cole, S., Lacey, C. G., Baugh, C. M., & Frenk, C. S. 2000, MNRAS, 319, 168
Cresci, G., & Maiolino, R. 2018, NatAs, 2, 179
Daddi, E., Dickinson, M., Morrison, G., et al. 2007, ApJ, 670, 156
Decarli, R., Walter, F., Aravena, M., et al. 2016, ApJ, 833, 70
Diamond-Stanic, A. M., & Rieke, G. H. 2010, ApJ, 724, 140
Ellison, S. L., Mendel, J. T., Patton, D. R., & Scudder, J. M. 2013, MNRAS, 435, 3627
Förster Schreiber, N. M., Roussel, H., Sauvage, M., & Charmandaris, V. 2004, A&A, 419, 501
Genzel, R., Tacconi, L. J., Gracia-Carpio, J., et al. 2010, MNRAS, 407, 2091
Greenhouse, M. A., Woodward, C. E., Thronson, H. A. J., et al. 1991, ApJ, 383, 164
Gross, A. C., Chen, Y.-C., Foord, A., et al. 2023, ApJ, 956, 117
Hartigan, P., Raymond, J., & Pierson, R. 2004, ApJL, 614, L69
Hill, M. J., & Zakamska, N. L. 2014, MNRAS, 439, 2701
Hopkins, P. F., Hernquist, L., Cox, T. J., & Kereš, D. 2008, ApJS, 175, 356
Hughes, D. H., Serjeant, S., Dunlop, J., et al. 1998, Natur, 394, 241
Hwang, H.-C., Shen, Y., Zakamska, N., & Liu, X. 2020, ApJ, 888, 73
Inada, N., Oguri, M., Shin, M.-S., et al. 2012, AJ, 143, 119
Ishikawa, Y., Zakamska, N. L., Shen, Y., et al. 2024, arXiv:2403.08098
Junkkarinen, V., Shields, G. A., Beaver, E. A., et al. 2001, ApJL, 549, L155
Kennicutt, R. C., & Evans, N. J. 2012, ARA&A, 50, 531
Kennicutt, R. C. J. 1998, ARA&A, 36, 189
Kim, J. H., Im, M., Lee, H. M., et al. 2012, ApJ, 760, 120
King, A. 2005, ApJL, 635, L121
Knapen, J. H., Cisternas, M., & Querejeta, M. 2015, MNRAS, 454, 1742
Kormendy, J., & Ho, L. C. 2013, ARA&A, 51, 511
Labiano, A., Argyriou, I., Álvarez-Márquez, J., et al. 2021, A&A, 656, A57
Lai, T. S. Y., Smith, J. D. T., Baba, S., Spoon, H. W. W., & Imanishi, M. 2020, ApJ, 905, 55
Law, D. R. E., Morrison, J., Argyriou, I., et al. 2023, AJ, 166, 45
Lemon, C. A., Auger, M. W., McMahon, R. G., & Ostrovski, F. 2018, MNRAS, 479, 5060
Li, J., Liu, X., Shen, Y., et al. 2023, ApJL, 955, L16
Magnelli, B., Popesso, P., Berta, S., et al. 2013, A&A, 553, A132
Magorrian, J., Tremaine, S., Richstone, D., et al. 1998, AJ, 115, 2285
Mannucci, F., Pancino, E., Belfiore, F., et al. 2022, NatAs, 6, 1185
More, A., Oguri, M., Kayo, I., et al. 2016, MNRAS, 456, 1595
Moreno, J., Torrey, P., Ellison, S. L., et al. 2019, MNRAS, 485, 1320
Mouri, H., & Taniguchi, Y. 2000, ApJL, 534, L63
Navarro, J. F., Frenk, C. S., & White, S. D. M. 1996, ApJ, 462, 563
Nisini, B., Caratti o Garatti, A., Giannini, T., & Lorenzetti, D. 2002, A&A, 393, 1035
Papadopoulos, P. P., van der Werf, P., Xilouris, E., Isaak, K. G., & Gao, Y. 2012, ApJ, 751, 10
Pearson, W. J., Wang, L., Alpaslan, M., et al. 2019, A&A, 631, A51
Peeters, E., Spoon, H. W. W., & Tielens, A. G. G. M. 2004, ApJ, 613, 986
Pooley, D., Blackburne, J. A., Rappaport, S., & Schechter, P. L. 2007, ApJ, 661, 19
Puget, J. L., & Leger, A. 1989, ARA&A, 27, 161
Reach, W. T., Rho, J., Tappe, A., et al. 2006, AJ, 131, 1479
Richards, G. T., Strauss, M. A., Fan, X., et al. 2006, AJ, 131, 2766
Rieke, G. H., Wright, G. S., Böker, T., et al. 2015, PASP, 127, 584
Rigby, J., Perrin, M., McElwain, M., et al. 2023, PASP, 135, 048001
Robitaille, T., Ginsburg, A., Mumford, S., et al. 2023, astropy/reproject: v0.10.0, Zenodo, doi:10.5281/zenodo.7584411
Rodighiero, G., Daddi, E., Baronchelli, I., et al. 2011, ApJL, 739, L40
Rosenberg, M. J. F., van der Werf, P. P., & Israel, F. P. 2012, A&A, 540, A116
Rupke, D. S. N. 2014, FSFIT: Spectral Fitting for Integral Field Spectrographs, Astrophysics Source Code Library, ascl:1409.005
Rupke, D. S. N., Gültekin, K., & Veilleux, S. 2017, ApJ, 850, 40
Rupke, D. S. N., Schweitzer, M., Viola, V., et al. 2021, QUESTFIT: Fitter for mid-infrared galaxy spectra, Astrophysics Source Code Library, ascl:2112.002
Rupke, D. S. N., Wylezalek, D., Zakamska, N. L., et al. 2023, ApJL, 953, L26
Saitoh, T. R., Daisaka, H., Kokubo, E., et al. 2009, PASJ, 61, 481
Salpeter, E. E. 1955, ApJ, 121, 161
Schawinski, K., Lintott, C. J., Thomas, D., et al. 2009, ApJ, 690, 1672
Schechter, P. L., Morgan, N. D., Chehade, B., et al. 2017, AJ, 153, 219
Schmidt, M. 1959, ApJ, 129, 243
Shang, Z., Brotherton, M. S., Wills, B. J., et al. 2011, ApJS, 196, 2
Shangguan, J., Ho, L. C., Bauer, F. E., Wang, R., & Treister, E. 2020, ApJ, 899, 112
Shen, Y., Chen, Y.-C., Hwang, H.-C., et al. 2021, NatAs, 5, 569
Shen, Y., Hwang, H.-C., Zakamska, N., & Liu, X. 2019, ApJL, 885, L4
Shi, Y., Ogle, P., Rieke, G. H., et al. 2007, ApJ, 669, 841
Shipley, H. V., Papovich, C., Rieke, G. H., Brown, M. J. I., & Moustakas, J. 2016, ApJ, 818, 60
Silva, A., Marchesini, D., Silverman, J. D., et al. 2018, ApJ, 868, 46

Smith, J. D. T., Draine, B. T., Dale, D. A., et al. 2007, ApJ, 656, 770
Solomon, P. M., & Vanden Bout, P. A. 2005, ARA&A, 43, 677
Spilker, J. S., Phadke, K. A., Aravena, M., et al. 2023, Natur, 618, 708
Tacconi, L. J., Genzel, R., Smail, I., et al. 2008, ApJ, 680, 246
Tang, S., Silverman, J. D., Ding, X., et al. 2021, ApJ, 922, 83
Vayner, A., Zakamska, N. L., Ishikawa, Y., et al. 2023, ApJ, 955, 92
White, S. D. M., & Frenk, C. S. 1991, ApJ, 379, 52
Wu, Y., Helou, G., Armus, L., et al. 2010, ApJ, 723, 895
Wylezalek, D., Vayner, A., Rupke, D. S. N., et al. 2022, ApJL, 940, L7
Xie, Y., & Ho, L. C. 2019, ApJ, 884, 136
Yu, Q. 2002, MNRAS, 331, 935
Zakamska, N. L., Lampayan, K., Petric, A., et al. 2016, MNRAS, 455, 4191